9-2012

Evidence for Low-Angle Normal Faulting in the Pumqu-Xianza Rift, Tibet

Patrick W. Monigle
Oregon State University

John Nabelek
Oregon State University

Jochen Braunmiller
Oregon State University, jbraunmiller@usf.edu

N. Seth Carpenter
Oregon State University

Geophysical Journal International

Geophys. J. Int. (2012) **190,** 1335–1340 doi: 10.1111/j.1365-246X.2012.05581.x

Evidence for low-angle normal faulting in the Pumqu-Xianza Rift, Tibet

Patrick W. Monigle, John Nabelek, Jochen Braunmiller, and N. Seth Carpenter*

College of Earth, Ocean, and Atmospheric Sciences, Oregon State University, Corvallis, OR 97331*, USA. E-mail: pmonigle@coas.oregonstate.edu*

Accepted 2012 June 15. Received 2012 June 11; in original form 2012 February 8

SUMMARY

Low-angle normal faulting is widely discussed as a possible mechanism for continental extension, however, unambiguous evidence for seismogenic low-angle normal faulting is lacking. Here, we investigate seismicity along a short segment of the Pumqu-Xianza Rift (PXR) in southern Tibet, where the HiCLIMB seismic array recorded over 500 earthquakes between 2004 July and 2005 August. Hypocentres of the 40 best recorded earthquakes are approximately 20–25 km west of the rift and tightly clustered at about 10 km depth, consistent with moment tensor depths of the 11 largest ($3.4 \leq M_w \leq 4.5$) earthquakes. Events in this group have N–S striking normal faulting mechanisms with low-angle (29°) west dipping fault planes. Rupture along a west dipping, low-angle, planar normal fault (the eastern PXR boundary fault) is consistent with event hypocentres, fault dip from moment tensors, and prominent surface morphology. The dip of 29° is at the low end of physically possible values assuming normal frictional behaviour and state of stress. We suggest it is possible for a planar, low-angle fault to nucleate seismically at a low angle at depth in the presence of basal shear and work its way aseismically through the brittle crust to the surface with the aid of lubricating minerals.

Key words: Seismicity and tectonics; Continental tectonics: extensional; Dynamics and mechanics of faulting.

1 INTRODUCTION

Under Andersonian stress distribution (Anderson 1951) and Coulomb rock strength conditions, brittle normal faults should initiate with dips of about 60°. For previously faulted rocks, following Byerlee's (1978) friction law, the range of possible normal-fault dips is substantially larger. A limiting frictional lock-up is expected to occur at about 30° dip (Sibson 1985). Global compilations of focal mechanisms of normal-faulting earthquakes with unambiguously identified fault planes show dip angles between 40° and 60° and only a few documented cases exist in the 30°–40° range (Doser 1987; Jackson & White 1989; Abers *et al.* 1997; Collettini & Sibson 2001). However, low-angle normal faults with dips smaller than 30° have been observed in surface geology and in seismic reflection profiles at shallow depths in the upper crust (e.g. Lister & Davis 1989; Wernicke 1995). It has been suggested these faults have been rotated from an initial steeper angle by flexure due to isostatic response (Buck 1988; Spencer & Chase 1989) or they are the result of departures from Andersonian stress distribution at depth (Melosh 1990; Westaway 1999).

Shallow seismicity in the Lhasa Block in southern Tibet occurs primarily along N–S trending grabens. Elliott *et al.* (2010) analysed teleseismic body wave and InSAR data from larger ($M_w \geq 5.9$) normal-faulting earthquakes to address their fault geometry and found fault planes with 40°–50° dips. Here, we investigate vigorous seismicity associated with the Pumqu-Xianza Rift (PXR) (earlier noted by Langin *et al.* 2003) recorded by the HiCLIMB seismic array between 2004 July and 2005 August, when the station distribution provides azimuthal coverage for accurate hypocentre determination (Fig. 1; Nabelek *et al.* 2009). During these 14 months, over 500 well-located events occurred in the PXR region (Fig. 1; Carpenter *et al.* 2010).

The PXR extends south from the Gyaring Co transform fault, across the Yarlung-Tsangpo Suture (YTS), to the Pumqu River, which it follows to the Himalayan range (Armijo *et al.* 1986). High seismicity during HiCLIMB occurred along a 16 km well-formed section of the PXR near the village of Qingdu (Fig. 1). Recent PXR earthquake activity (ISC $m_b \geq 4.0$) began in 1980 with an M_w 6.4 event near the northern end of the graben, followed by aftershocks and sporadic activity through the mid 1980's. Seismicity returned in 1994, with activity clustered south of the 1980's events including M_w 5.7 and 5.9 events in 1996 and 1998. The Qingdu segment has been active since 1994 and the last two reported earthquakes occurred in 2010. We use HiCLIMB data to relocate the 50 best recorded earthquakes ($2.1 \leq M_L \leq 5.0$) and to determine 12 regional moment tensors (RMT). Our results provide evidence for active, low-angle (29°) normal faulting.

*Now at: Kentucky Geological Survey, Lexington, KY 40506, USA.

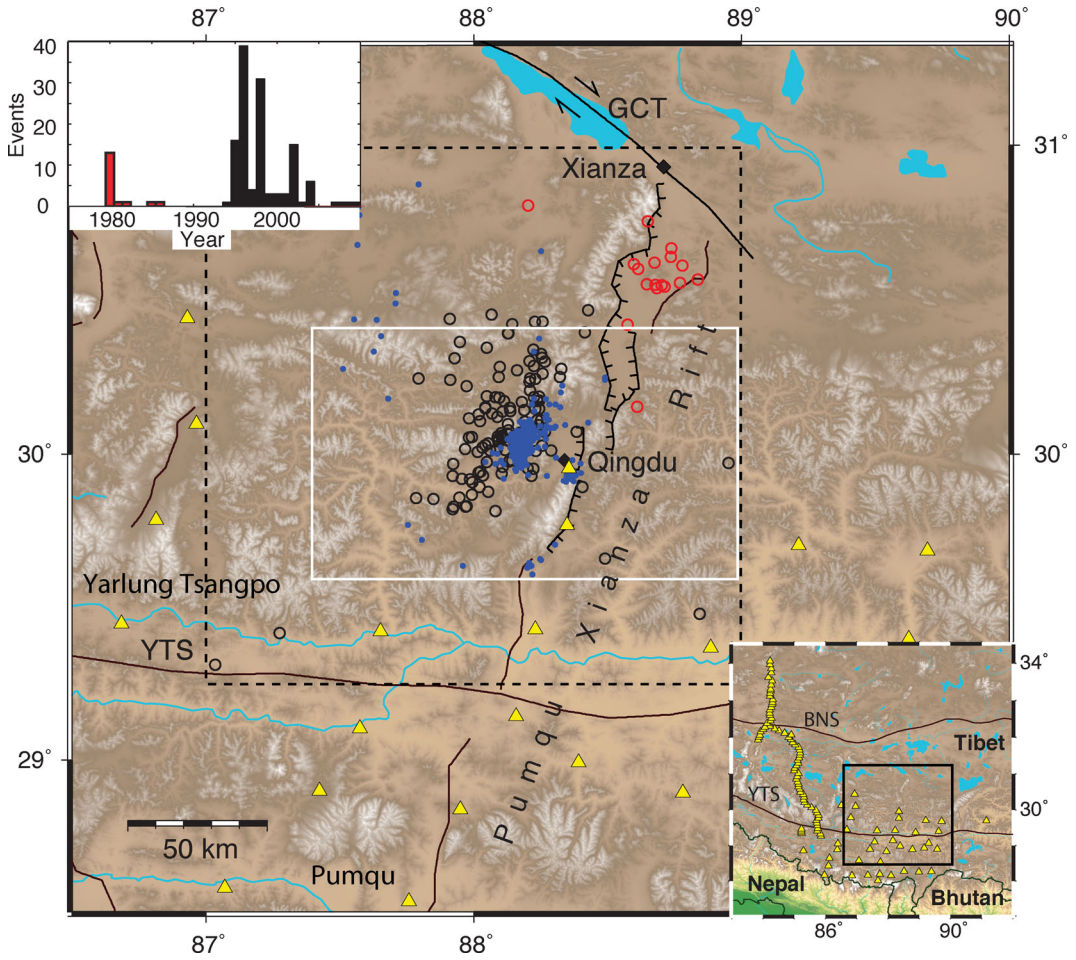

Figure 1. Map of the Pumqu-Xianza Rift. PXR fault scarps were identified from satellite imagery; tick marks indicate clear hangingwall slip directions. Gyaring Co Transform fault (GCT) and Yarlung-Tsangpo Suture (YTS) are also plotted. Nearby HiCLIMB seismic stations indicated by yellow triangles. International Seismological Center (ISC) earthquake locations are shown as open circles (red: 1980s, black: 1994–2012). Blue dots are epicentres from the Carpenter *et al.* (2010) HiCLIMB catalogue within the black-dashed box. Black diamonds are towns. White box is area of Fig. 2. Upper inset shows histogram of ISC reported ($m_b \geq 4.0$) seismicity. Lower inset shows HiCLIMB phase-2 stations; YTS and BNS (Bangong-Nujiang Suture) bound the Lhasa Block. Black box shows the area of the main figure.

2 DATA ANALYSIS

Earthquakes were selected from the catalogue of Carpenter *et al.* (2010) (Fig. 1), which is based on automatic phase picks from the HiCLIMB phase-2 deployment (Fig. 1 inset). The catalogue lists over 500 well-located earthquakes (with at least 20 *P* and *S* arrivals) in the study area. Forty earthquakes with more than 35 *P* and *S* arrivals were selected from the cluster west of Qingdu and 10 additional events based on their proximity to stations south of Qingdu. *P* and *S* arrivals for each event were inspected and adjusted manually; numerous *P* and *S* arrivals were added. On average, manually located events show only a small southwestward shift of 2.2 km (standard deviation: 1.8 km) from the Carpenter *et al.* (2010) catalogue.

Earthquake hypocentres (Fig. 2; Table S1) were determined by least-squares traveltime inversion using GENLOC (Pavlis *et al.* 2004). Uniform *P*- and *S*-wave arrival uncertainties were assigned based on overall pick uncertainty (0.2 and 0.5 s, respectively) and distance weighting was implemented with full weighting of arrivals to 2° distance, reducing linearly to zero weight beyond 3° distance. We used two crust/upper mantle velocity models (Fig. S1): a receiver function model for this region (Nabelek *et al.* 2009) and a

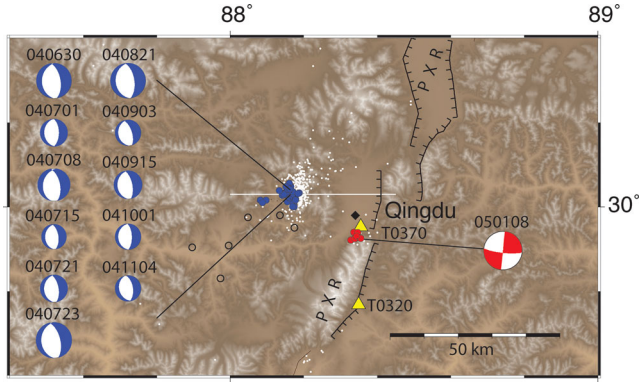

Figure 2. Epicentres for manually located earthquakes, blue for events west of the Qingdu segment and red for events near station T0370. White dots are epicentres from the Carpenter *et al.* (2010) HiCLIMB catalogue. White line shows profile location for Fig. 3. Fault plane solutions from RMT analysis are identified by event date (YYMMDD) and colour-coded by faulting type. Complete results are provided in the electronic supplement. Teleseismic ISC locations for six earthquakes (black circles) relocate into the blue cluster. Delineated faults are as in Fig. 1.

traveltime-based model calculated from P_g, P_n, S_g and S_n arrivals identified in this study. Hypocentre locations were similar for both models. Tests using different starting depths produced essentially identical results. The mean horizontal error ellipse ($1-\sigma$) has a major axis of 1.7 km (max. 3.0 km) and minor axis of 0.8 km, striking 40°; the depth error is 0.5 km (max. 1.1 km). The combination of *P* and *S* arrivals from the closest stations and P_n phases control the estimated depth. The maximum station azimuthal gap is 155° (no coverage at azimuths 300° to 95°) for events west of Qingdu and less than 90° for events south of Qingdu.

In all, 40 events were located in a cluster 20–25 km west from the east-wall fault scarp of the PXR (Fig. 2). These events range from 6 to 12 km depth, with a lateral spread of 5 km east–west and 6 km north–south. Double-difference relative locations (Waldhauser & Ellsworth 2000) exhibit a similar tight cluster. We found no discernible temporal event migration pattern. Another seven events, at 6–9 km depth, were located within the PXR valley near station T0370 and three small events ($2.2 \leq M_L \leq 2.5$) occurred further south near T0320.

RMT solutions were determined from complete three-component seismograms (Fig. S2 and Table S2) following Nabelek & Xia (1995). The receiver function model was reduced to a slowness-balanced, eight-layer model for RMT calculations (Fig. S1) and results with the traveltime-based model were essentially identical. Moment tensors were constrained to be deviatoric and data were weighted based on epicentre-station azimuth, with equal weight for each 30° sector.

RMT analysis was performed on 12 earthquakes ($3.2 \leq M_w \leq 4.5$). Eleven events in the cluster west of the graben (Fig. 2) were analysed in the 20–50 s band with, on average, 47 seismograms. They have normal faulting mechanisms with mean nodal planes of 179°/29°/−82° and 351°/61°/−94° (strike/dip/rake). Dip is the best-resolved parameter and for the best constrained events dip uncertainty, based on conservative 5 per cent variance increase, is between 3° and 4°. Analysis in the 10–30 s band on these 11 events gave similar results, with a slight decrease in dip for the west-dipping nodal planes (mean: 180°/23°/−88°). The smallest event occurred inside the graben near T0370 and could only be analysed in the 10–30 s band. This event has a strike-slip mechanism.

3 DISCUSSION

The northern PXR is variably expressed (Figs 1 and 2). At its north end, near Xianza, the western wall is a prominent fault scarp, while to the east no clear valley-bounding fault exists. As the PXR approaches the Qingdu segment from the north, the eastern wall becomes a sharp bounding fault, while the western boundary becomes structurally subdued. At about 30.1°N, the PXR steps west into the Qingdu segment, which is a 16 km long and 8–10 km wide half-graben with an apparent bounding fault on the eastern side of the valley. Immediately south of Qingdu and T0370, the eastern wall of the Qingdu valley terminates; its continuation becomes a prominent fault of an east dipping half-graben.

Seismicity since 1994 (Fig. 1) is focused on the Qingdu region (29.7°–30.3°N), but well west of the valley and with diffuse activity continuing north and south of the actual Qingdu segment. During the HiCLIMB deployment, seismicity was high, tightly clustered 20–25 km west of the east-bounding wall of the PXR and focused on the Qingdu segment (Fig. 2). Relocation places the six earthquakes listed in the ISC catalogue into this tight cluster, suggesting the full spread of ISC events (as shown in Fig. 1) may not be accurate, though their overall westward shift relative to the PXR is probably real.

Based on our relocations and the Carpenter *et al.* (2010) catalogue, the entire Qingdu segment was seismically active during the HiCLIMB deployment (Fig. 2). The north–south extent of seismicity appears to be bound by the Qingdu segment boundaries. The events are west of the rift and have normal faulting mechanisms with N–S striking nodal planes. Hypocentres are at 9–12 km depths from location and moment tensor analysis. Nodal plane dips, well resolved from waveform modelling (Fig. S2), indicate rupture either on a shallow 29° westward dipping fault or on a 61° steeply eastward-dipping fault.

In addition to high seismicity west of the rift, several small ($M_w \leq 3.2$) earthquakes occurred directly under the half-graben just south of T0370 (Fig. 2). The single RMT solution established for these events is strike-slip, suggesting they could represent E–W transform motion between the footwalls of west and east dipping normal faults as the PXR steps east south of Qingdu, consistent with current motion on these main faults.

Fig. 3 shows possible faulting interpretations consistent with RMT solutions and hypocentre locations. Our preferred interpretation is that the earthquakes west of the PXR occurred along a planar, west-dipping, low-angle (dip 29°) normal fault surfacing at the eastern boundary wall of the PXR, a prominent fault scarp on satellite imagery. The earthquake hypocentres are just above the top of a low-velocity zone imaged by receiver functions (Nabelek *et al.* 2009) and near the base of the brittle upper crust. This is the simplest

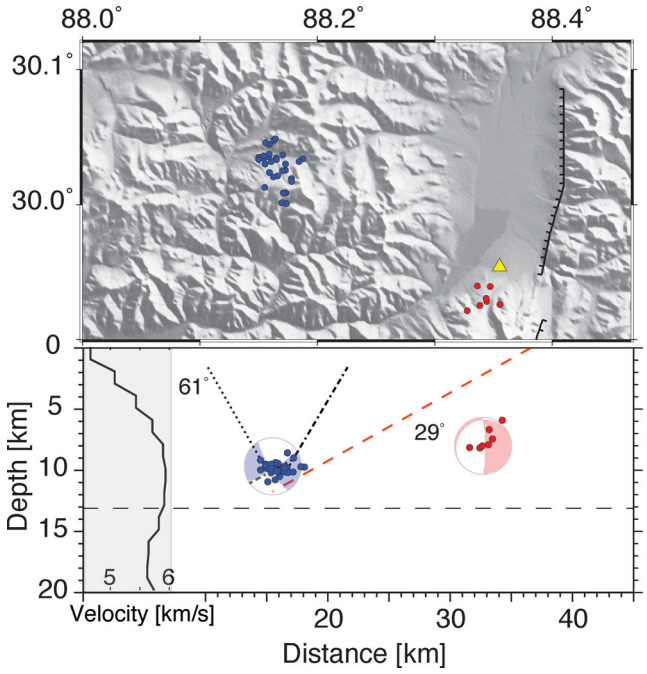

Figure 3. Shaded relief map highlighting topography (top panel) and possible tectonic interpretations (bottom panel). Highest quality hypocentres (best geometrical coverage) follow Fig. 2 colour scheme. Receiver function velocity model from Nabelek *et al.* (2009) is embedded to the left within profile view. Horizontal black dashed line marks the top of the low-velocity zone, likely corresponding to base of the seismogenic upper crust. Possible faulting interpretations illustrated: planar 29° west dipping low-angle fault surfacing at the PXR east wall (red dashed line), west dipping listric fault (black dash-dotted line), and planar high-angle 61° east dipping fault (black dotted line). Only the 29° west dipping fault interpretation is associated with a surface expression.

interpretation that geometrically connects seismic observations at depth with surface morphology.

We cannot, however, preclude other interpretations because slip from none of the earthquakes ($M_w \leq 4.5$), with faulting dimensions of about 1 km^2, reached the surface and because the hypocentres do not define a fault plane. The events could have occurred on a minor fault with no surface expression and not associated with the PXR. A west dipping listric fault (dash-dotted line in Fig. 3) or a steep (61°) east dipping fault (dotted line in Fig. 3), both west of the PXR, cannot be ruled out. Activity along previously unmapped faults or faults without obvious geomorphic surface expression has been documented for several normal faulting earthquakes in Tibet (M_w 5.9–6.4) with high-angle fault plane solutions (40°–50°) by Elliott *et al.* (2010).

However, the following observations combined support the interpretation that the seismicity described here is related to the west dipping eastern bounding fault of the Qingdu segment: (1) The earthquakes have hypocentres and moment tensor mechanisms consistent with a planar fault reaching the surface at the eastern side of the Qingdu valley; (2) The eastern fault scarp in the Qingdu valley is a dominant feature indicating Holocene movement; (3) Seismicity correlates with the north–south length of the Qingdu valley; (4) Transform-fault events inside the Qingdu valley indicate active motion on the main PXR normal faults.

Seismogenic normal faulting along crustal-scale faults dipping 40° or less has been documented only in a few cases, with dips near or below 30° being extremely rare (Jackson & White 1989; Collettini & Sibson 2001). The most striking examples come from earthquakes within the Woodlark basin (Abers 1991; Abers *et al.* 1997) where body wave modelling indicates 24°–35° dips for several events; a 32° dip for a 1970 event near Moresby Seamount is supported by independent seismic reflection data. Shallow fault dips have also been found for earthquakes in the western Gulf of Corinth with 30° ± 5° for the 1995 Aigion earthquake (Bernard *et al.* 1997) and 30° ± 3° for the 1992 Galaxidi earthquake (Hatzfeld *et al.* 1996), but not for events in the eastern part of the gulf, which dip near 40° (Braunmiller & Nabelek 1996). The 1946 Ancash, Peru earthquake is possibly another example for 30° normal faulting (Doser 1987). Surface ruptures were mapped near, but not on, pre-existing thrust faults dipping 25°–35°, with the main surface scarp from the earthquake dipping at 42° (Doser 1987). Given the limited waveform data available, dip uncertainty could be larger than the 10° reported. Detachment faults dipping 0°–20° have been observed geologically (Wernicke 1995), but whether such faults slip seismically is not clear. Eyidogan & Jackson (1985) modelled waveform complexities for events in western Turkey as subhorizontal detachment faulting, though reanalysis by Braunmiller & Nabelek (1996) shows the events are planar with dips near 40°.

The physical processes driving low-angle faulting are poorly understood. Frictional lock-up, prohibiting further slip on pre-existing faults, is expected to occur at about 30°–40° dip for Andersonian stress distribution and a typical coefficient of friction near 0.6 (Fig. 4; Sibson 1985; Collettini & Sibson 2001). Slip on faults shallower than 30° requires stress-field rotation (Melosh 1990; Westaway 1999) or fault weakening, possibly through a combination of a lower friction coefficient μ and increased pore pressure (Collettini & Sibson 2001).

The dips for the PXR events, assuming they occurred on the west dipping fault, range from 22° to 33° (mean value 29°), which, at 22°, would be locked-up. The top of a low-velocity zone (Nabelek *et al.* 2009) at 15–20 km depth in the Lhasa Block probably defines the base of the seismogenic zone. Shear at this base may rotate the

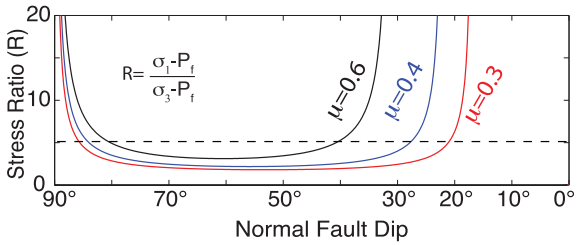

Figure 4. Ratio of effective principal stresses (R) for reactivation of a cohesionless fault plotted against normal fault dip (after Collettini & Sibson 2001) for vertical principal stress (σ_1). For normal friction, $\mu = 0.6$, a fault dipping ≤30° is completely locked and cannot move; slip on faults dipping between 30° and 40° requires high stress ratios making slip less likely as dip decreases. A reduction to $\mu = 0.3$–0.4 is necessary to accommodate slip along faults with 22°–33° dip. Dashed line indicates approximate dip limit for active slip, about 40° under normal conditions ($\mu = 0.6$), as indicated by global observations.

stress-field (Westaway 1999) enabling seismic activity along a low-angle normal fault at the base of the brittle crust as observed here. The cause for basal shear could be traction from the subhorizontal motion of the Indian Plate along the Main Himalayan Thrust (MHT; McCaffrey & Nabelek 1998), which is at about 45 km depth in the Lhasa Block (Nabelek *et al.* 2009); this traction requires a well-coupled plate interface and a high-viscosity middle crust above the interface (Copley *et al.* 2011).

At shallower depths, significant deviations from Andersonian stress distribution are unlikely and to extend seismic slip along a low-angle fault to the surface requires a weak fault. This could be achieved by geothermally driven increased pore fluid pressure and/or a reduction of friction along the fault zone to $\mu = 0.3$–0.4 (Fig. 4). High heat flow and abundant geothermal activity are associated with grabens in Tibet (Armijo *et al.* 1986). Fluid presence would aid chemical weathering leading to deposits of weak phyllosilicates (e.g. clay, talc) in a fault zone. Fault material containing the clay mineral smectite with $\mu = 0.21$ was found at 2.7 km depth on the San Andreas Fault in a segment characterized by stable creep (Carpenter *et al.* 2011). Talc has a friction coefficient of 0.1–0.2 and is stable over a wide temperature range (Moore & Lockner 2008) and hence it can be potentially present over a wide depth range within a fault zone. Phyllosilicates, however, exhibit velocity strengthening frictional behaviour and their presence would result in aseismic creep rather than seismic slip on a fault.

Low-angle (∼30°) normal faults have been also identified in the shallow crust in the Lunggar rift (Kapp *et al.* 2008) and the Yadong-Gulu rift (Cogan *et al.* 1998) in the Lhasa Block. So far, it has not been determined how deep the shallow-dipping parts of these faults extend or if they are seismogenic. The Yadong-Gulu rift fault has been interpreted in terms of a rolling-hinge model with a steeper, active part extending into the deeper seismogenic zone (Cogan *et al.* 1998). The Lunggar rift is described as an evolutionary structure that initiated as a steep fault and subsequently rotated into its present 30° dip (Kapp *et al.* 2008). We suggest that a planar, 30°-dip fault can be created without rotation from initially steep inclination under special conditions: shear traction at the base of the seismogenic layer and an environment conducive to the generation of phyllosilicates. Initiating at the base of the brittle crust in a seismic fashion, in the presence of a basal traction, low-angle faulting may work its way to the surface by creep enabled through fluid influx progressively lining the developing fault interface with lubricating minerals. For a creeping, lubricated fault we would expect substantially

reduced numbers of higher magnitude earthquakes (Amelung & King 1997).

4 CONCLUSION

Our study is one of few to support low-angle normal faulting from earthquake source mechanisms. We provide evidence for faulting with dips in the range of 22°–33° from well-resolved earthquake RMT solutions. Combined with the hypocentre locations, such faulting is consistent with activity on the west dipping eastern PXR fault, which shows prominent surface morphology. The dips are at the low end of or below physically possible values assuming normal frictional behaviour (Collettini & Sibson 2001). The earthquakes occurred near the base of the seismogenic layer (Nabelek *et al.* 2009). Traction at the base of the seismogenic layer transmitted upwards from the MHT (McCaffrey & Nabelek 1998; Copley *et al.* 2011) may rotate the stress field to enable brittle, low-angle normal slip. To extend slip along a low-angle normal fault to the surface requires a decrease in effective fault friction (strength), which may be achieved by lining the fault with phyllosilicates and/or by increasing the fluid pressure in the fault zone. The presence of phyllosilicates, though, would probably render slip in the upper fault zone aseismic, at least for crustal-scale earthquakes. Our results from PXR indicate that 30° planar faults can form and extend across the entire brittle crust in the Lhasa Block.

ACKNOWLEDGMENTS

This study was supported by the NSF, Continental Dynamics Program, grant EAR 9909609 and the Air Force Research Laboratory, contract FA8718–09-C-0004. The authors wish to thank C. Collettini and two anonymous reviewers for comments.

REFERENCES

Abers, G.A., 1991. Possible seismogenic shallow-dipping normal faults in the Woodlark-D'Entrecasteaux extensional province, Papua New Guinea, *Geology,* **19,** 1205–1208.

Abers, G.A., Mutter, C.Z. & Fang, J., 1997. Shallow dips of normal faults during rapid extension: earthquakes in the Woodlark-D'Entrecasteaux rift system, Papua New Guinea, *J. geophys. Res.,* **102,** 15 301–15 317.

Amelung, F. & King, G., 1997. Earthquake scaling laws for creeping and non-creeping faults, *Geophys. Res. Lett.,* **5,** 507–510.

Anderson, E.M., 1951. *The Dynamics of Faulting and Dyke Formation,* Oliver and Boyd, Edinburgh, 206pp.

Armijo, R., Tapponnier, P., Mercier, J.L. & Tong-Lin, H., 1986. Quaternary extension in southern Tibet: field observations and tectonic implications, *J. geophys. Res.,* **91,** 13803–13872.

Bernard, P. *et al*., 1997. The $M_s = 6.2$, June 15, 1995 Aigion earthquake (Greece): evidence for low angle normal faulting in the Corinth rift, *J. Seismol.,* **1,** 131–150.

Byerlee, J., 1978. Friction of rocks, *Pure appl. Geophys.,* **116,** 615–626.

Braunmiller, J. & Nabelek, J., 1996. Geometry of continental normal faults: seismological constraints, *J. geophys. Res.,* **101,** 3045–3052.

Buck, W.R., 1988. Flexural rotation of normal faults, *Tectonics,* **7,** 959–973.

Carpenter, S., Nabelek, J. & Braunmiller, J., 2010. South-central Tibetan seismicity from HiCLIMB seismic array data, *EOS, Trans. Am. geophys. Un.,* **91,** Fall Meeting Suppl., Abstract T43B-2223.

Carpenter, B.M., Marone, C. & Saffer, D.M., 2011. Weakness of the San Andreas Fault revealed by samples from active fault zones, *Nat. Geosci.,* **4,** 251–254.

Cogan, M.J., Nelson, K.D., Kidd, W.S.F., Wu, C., Project INDEPTH Team, 1998. Shallow structure of the Yadong-Gulu ridf, southern Tibet, from refraction analusis of Project INDEPTH common midpoint data, *Tectonics,* **17,** 46–61.

Copley, A., Avouac, J.-P. & Wernicke, B.P., 2011. Evidence for mechanical coupling and strong Indian lower crust beneath southern Tibet, *Nature,* **472,** doi:10.1038/nature09926.

Collettini, C. & Sibson, R.H., 2001. Normal faults, normal friction?, *Geology,* **29,** 927–930.

Doser, D.I., 1987. The Ancash, Peru, earthquake of 1946 November 10: evidence for low-angle normal faulting in the high Andes of northern Peru, *Geophys. J. R. astr. Soc.,* **91,** 57–71.

Elliott, J.R., Walters, R.J., England, P.C., Jackson, J.A., Li, Z. & Parsons, B., 2010. Extension on the Tibetan plateau: recent normal faulting measured by InSAR and body wave seismology, *Geophys. J. Int.,* **183,** 503–535.

Eyidogan, H. & Jackson, J., 1985. A seismological study of normal faulting in the Demirci, Alasehir and Gediz earthquakes of 1969–70 in western Turkey: implications for the nature and geometry of deformation in the continental crust, *Geophys. J. R. astr. Soc.,* **81,** 569–607.

Hatzfeld, D. *et al*., 1996. The Galaxidi earthquake of 18 November 1992: a possible asperity within the normal fault system of the Gulf of Corinth (Greece), *Bull. seism. Soc. Am.,* **86,** 1987–1991.

Jackson, J.A. & White, N.J., 1989. Normal faulting in the upper continental crust: observations from regions of active extension, *J. Struct. Geol.,* **11,** 15–36.

Kapp, P., Taylor, M., Stockli, D. & Ding, L., 2008. Development of active low-angle normal fault systems during orogenic collapse: insight from Tibet, *Geology,* **36,** 7–10.

Langin, W.R., Brown, L.D. & Sandvol, E., 2003. Seismicity of central Tibet from Project INDEPTH III seismic recordings, *Bull. seism. Soc. Am.,* **93,** 2146–2159.

Lister, G.S. & Davis, G.A., 1989. The origin of metamorphic core complexes and detachment faults formed during the Tertiary continental extension in the northern Colorado River region, USA, *J. Struct. Geol.,* **11,** 65–93.

McCaffrey, R. & Nabelek, J., 1998. Role of oblique convergence in the active deformation of the Himalayas and southern Tibet plateau, *Geology,* **26,** 691–694.

Melosh, H.J., 1990. Mechanical basis for low-angle normal faulting in the Basin and Range province, *Nature,* **43,** 331–335.

Moore D.E. & Lockner, D.A., 2008. Talc friction in the temperature range 25°-400°C: relavance for fault-zone weakening, *Tectonophysics,* **449,** 120–132.

Nabelek, J. & Xia, G., 1995. Moment-tensor analysis using regional data: application to the 25 March, 1993, Scotts Mills, Oregon, earthquake, *Geophys. Res. Lett.,* **22,** 13–16.

Nabelek, J. *et al*., 2009. Underplating in the Himalaya-Tibet collision zone revealed by the Hi-CLIMB experiment, *Science,* **325,** 1371–1374.

Pavlis, G.L., Vernon, F., Harvey, D. & Quinlan, D., 2004. The generalized earthquake-location (GENLOC) package: An earthquake-location library, *Comput. Geosci.,* **30,** 1079–1091.

Sibson, R.H., 1985. A note on fault reactivation, *J. Struct. Geol.,* **7,** 751–754.

Spencer, J.E. & Chase, C.G., 1989. Role of crustal flexure in initiation of low-angle normal faults and implications for structural evolution of the Basin and Range province, *J. geophys. Res.,* **94,** 1765–1775.

Waldhauser, F. & Ellsworth, W.L., 2000. A double-difference earthquake location algorithm: method and application to the Northern Hayward Fault, California, *Bull. seism. Soc. Am.,* **90,** 1353–1368.

Wernicke, B., 1995. Low-angle normal faults and seismicity: a review, *J. geophys. Res.,* **100,** 20159–20174.

Westaway, R., 1999. The mechanical feasibility of low-angle normal faulting, *Tectonophysics,* **308,** 407–443.

SUPPORTING INFORMATION

Additional Supporting Information may be found in the online version of this article:

Figure S1. Velocity models used for hypocentre and RMT determination: receiver function model from Nabelek *et al.* (2009) (black),

eight-layer model retaining receiver function overall layer slowness (red), and model based on P_g and P_n traveltimes (green).

Figure S2. Example of RMT inversion for event 040723_0125. Observed (black) and synthetic (red) seismograms for a few select stations in each 30° azimuthal sector used for inversion. Right shows variance of fit as a function of depth (bottom panel) and changes in strike, dip and rake relative to the best double couple solution (179°/29°/−82°) (top panel). Confidence intervals mentioned in the text and listed in Table S2 are based on a conservative 5 per cent variance increase. Triangles along the circumference of the focal mechanism on bottom show azimuthal station distribution, red triangles are stations shown above.

Table S1. Hypocentre locations of 50 earthquakes in the PXR region determined in this study using the receiver function velocity model (Fig. S1). Columns are: Event date, time, latitude, longitude, depth, number of *P* and *S* arrivals used, horizontal $1-\sigma$ error ellipse (columns 7 to 9), and local magnitude. We utilized 105 broad-band and 3 short-period stations with sample rates of 50 or 100 Hz. For the three earliest events, not all close-by stations were operating resulting in larger uncertainties. Their apparent slight west-shift (see also Fig. 2) is an artefact; hypoDD relative location (Waldhauser & Ellsworth 2000) moved these events east into the remaining cluster. Station outages beginning in 2004 November reduced near-by coverage for seven western cluster events. We do not show these 10 events in Fig. 3.

Table S2. Source parameters of 12 earthquakes from regional moment tensor (RMT) analysis in the 20–50 s period band. Columns left to right are: event date and origin time; strike, dip and rake for nodal plane 1; uncertainties for nodal plane 1; strike, dip and rake for nodal plane 2; RMT depth; RMT depth uncertainty; moment magnitude; number of seismic stations used in RMT analysis; and percent double couple for each solution. Asterisk denotes the event analysed in the 10–30 s band. Uncertainties are based on 5 per cent variance increase.